

A simple model to describe intrinsic stellar noise for exoplanet detection around red giants

Thomas S. H. North,^{1,2*} William J. Chaplin,^{1,2} Ronald L. Gilliland,^{3,4}
 Daniel Huber,^{5,6,2} Tiago L. Campante,^{1,2} Rasmus Handberg,^{2,1} Mikkel N. Lund,^{1,2}
 Dimitri Veras,⁷ James S. Kuszlewicz,^{1,2} Will M. Farr¹,

¹*School of Physics and Astronomy, University of Birmingham, Birmingham, B15 2TT, United Kingdom*

²*Stellar Astrophysics Centre (SAC), Department of Physics and Astronomy, Aarhus University, Ny Munkegade 120, DK-8000 Aarhus C, Denmark*

³*Department of Astronomy and Astrophysics, and Center for Exoplanets and Habitable Worlds, The Pennsylvania State University, 525 Davey Lab, University Park, PA 16802, USA*

⁴*Space Telescope Science Institute, 3700 San Martin Dr., Baltimore, MD 21218, USA*

⁵*Sydney Institute for Astronomy (SIfA), School of Physics, University of Sydney, NSW 2006, Australia*

⁶*SETI Institute, 189 Bernardo Avenue, Mountain View, CA 94043, USA*

⁷*Department of Physics, University of Warwick, Coventry, CV4 7AL, United Kingdom*

Accepted XXX. Received YYY; in original form ZZZ

ABSTRACT

In spite of the huge advances in exoplanet research provided by the NASA *Kepler* Mission, there remain only a small number of transit detections around evolved stars. Here we present a reformulation of the noise properties of red-giant stars, where the intrinsic stellar granulation, and the stellar oscillations described by asteroseismology play a key role. The new noise model is a significant improvement on the current *Kepler* results for evolved stars. Our noise model may be used to help understand planet detection thresholds for the ongoing K2 and upcoming TESS missions, and serve as a predictor of stellar noise for these missions. As an application of our noise model, we explore the minimum detectable planet radii for red giant stars, and find that Neptune sized planets should be detectable around low luminosity red giant branch stars.

Key words: asteroseismology – techniques: photometric – planetary systems

1 INTRODUCTION

Red giants, stars near the end of their life – which have exhausted fusable hydrogen in the stellar core, and bloated massively compared to their main-sequence radii – are a relatively new focus for photometric exoplanet research. The four years of near continuous, high-quality photometry from the NASA *Kepler* Mission has been a key driver in studies of exoplanets, including close in planets around evolved stars (Huber et al. 2013; Steffen et al. 2013; Lillo-Box et al. 2014; Ciceri et al. 2015; Barclay et al. 2015; Quinn et al. 2015). Previous exoplanet searches around giant stars have primarily been conducted using radial velocity measurements (Johnson et al. 2008; Reffert et al. 2015; Quirrenbach et al. 2015).

One reason for the interest in red giants is that when the Sun reaches this stage of evolution the fate of the Earth is a contentious matter, with the ultimate balance between mass loss and the maximum extent of the Sun being the deciding factors (Schröder & Connon Smith 2008), along with the influence of tidal decay on the orbit. The timescales for dynamic evolution of the system are accelerated as the star evolves, with evidence of several planet hosts on course to devour their planets (Adamów et al. 2012); an example is Kepler-56, a red giant with two detected transiting planets that are predicted to be consumed by their star in around 150 million years (Li et al. 2014).

Kepler has provided high precision measurements of stellar variability, and a host of related phenomena, such as activity, stellar rotation (McQuillan et al. 2014) and the detection of intrinsic, oscillations in stars. The analysis of the detected oscillations – the field of asteroseismology – in principle provides very precise constraints on stellar properties,

* E-mail: txn016@bison.ph.bham.ac.uk (TSHN)

a key ingredient in the characterisation of exoplanets (Van Eylen et al. 2014). *Kepler* has observed solar-like oscillations in over 15,000 red giants (Hekker et al. 2011; Mosser et al. 2012a,b; Stello et al. 2013), another reason that a search for planets around giants is of interest. Asteroseismology may be used to discriminate between stars either ascending the red giant branch (RGB), or in the Helium core burning “red clump” (RC) phase (Bedding et al. 2011). This is particularly important for the possible detection, and existence, of close-in planets. Asteroseismic results on the stellar angle of inclination of the host star can also reveal if it is a misaligned system, where the stellar spin axis and plane of planetary orbits are not coplanar (Huber et al. 2013). Finally, asteroseismology also provides well-constrained stellar ages (Silva Aguirre et al. 2015), allowing star and planet formation to be probed across Galactic history (Campante et al. 2015).

The ability to detect a planetary transit is limited by multiple factors, the primary factor being the depth of the transit, which is directly related to the relative size of planet and host star. Another more subtle issue is the noise properties of the host star, which in cool main-sequence, sub-giant and red-giant stars can contain contributions from various stellar signals indicative of granulation, oscillations and activity. Additionally, there is a shot noise contribution to be considered and instrumental artefacts. Detecting the transit signal requires an understanding of the expected noise properties and the expected appearance of the transit in the lightcurve.

In this paper we present a simple model of the noise properties relevant to transit detection around red giants, which employs scaling relations based on global asteroseismic parameters. The dominant contributions are those due to granulation and solar-like oscillations. This model is then used to estimate minimum detectable planet radii for different assumed orbital periods.

Readers unfamiliar with asteroseismology will find an introduction to the relevant parameters in Section 2.1. The relevant parameters for the noise model are introduced in Section 2.2, and the current *Kepler* noise properties are discussed in Section 3. Finally, Section 4 covers the construction of the noise model and discusses the implications of the resulting predictions for detecting planets around red giants in *Kepler* data.

2 FREQUENCY SPECTRUM OF RED GIANTS: OSCILLATIONS AND GRANULATION

The noise model detailed below is based on observed stellar parameters. Given the close connection between stellar granulation and oscillations, where possible the individual parameters of the model for the oscillation and granulation components are described in terms of the asteroseismic parameters, along with additional fundamental stellar parameters, where appropriate.

We begin here by introducing the relevant asteroseismic parameters, and the intrinsic stellar properties they relate to. Those already familiar with asteroseismic parameters can skip to Section 2.2.

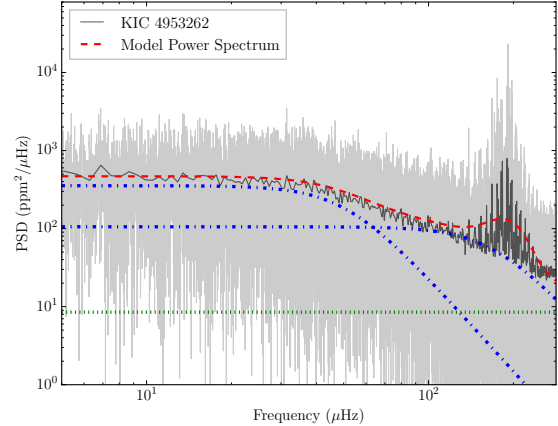


Figure 1. The power density spectrum for KIC 4953262, with the raw and smoothed power spectra in grey and black respectively. Green (dotted) indicates the shot noise level, showing it is a small factor for this star, whilst the blue (dashed dotted) show the two granulation components, red (dashed) is total model power spectrum including an oscillation component, where the individual modes are not modelled in this formulation.

2.1 Asteroseismic global parameters

Solar-like oscillations are driven and damped by turbulent convection in the outer envelope of the star, with the amplitudes of these signals greatly enhanced in evolved stars (Baudin et al. 2011). Figure 1 shows an example red-giant frequency power spectrum, made from *Kepler* data on the target KIC 4953262. The two main features of the power spectrum are the stellar granulation background, and solar-like oscillations. The oscillations are clearly visible above the background around 200 μHz. Additionally, model fits to the components are overplotted, and will be returned to in Section 2.2. For the noise model detailed in Section 4, the individual oscillation modes do not need to be modelled, only the oscillation power envelope that contains them.

Figure 2 shows a zoom of the same power spectrum, around the region where the detected stellar oscillations are most prominent. The oscillations appear as fairly evenly spaced peaks in frequency. Overtones of the same angular degree, l , are spaced by the large frequency separation. The average large separation, $\Delta\nu$, scales to good approximation with the square-root of mean stellar density (Ulrich 1986), i.e.,

$$\frac{\Delta\nu}{\Delta\nu_{\odot}} \simeq \left(\frac{M}{M_{\odot}}\right)^{0.5} \left(\frac{R}{R_{\odot}}\right)^{-1.5}. \quad (1)$$

The observed power of the mode peaks is modulated by an envelope that is usually taken as being a Gaussian, centered on the frequency ν_{\max} , i.e., the frequency at which the detected oscillations show their strongest amplitudes. This characteristic frequency can be predicted from fundamental parameters. Its physical meaning is still debated (Belkacem et al. 2011), but it scales to very good approximation with the (isothermal) acoustic cut-off frequency in the stellar atmosphere, with numerous studies showing

$$\nu_{\text{ac}} \propto \nu_{\max} \propto \frac{c}{H}. \quad (2)$$

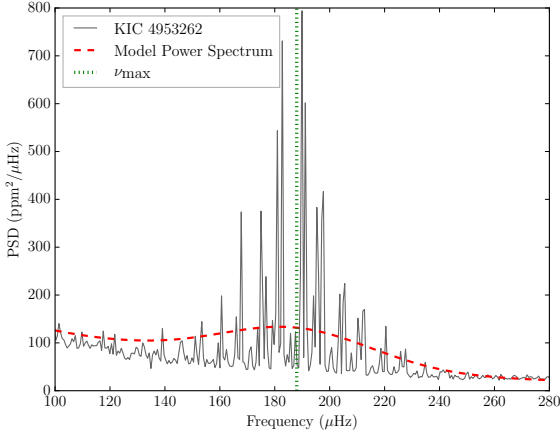


Figure 2. Smoothed power spectrum for KIC 4953262, a known oscillating red giant. The vertical dotted line indicates ν_{\max} for this star. Shown in red is a model of the power envelope of the oscillation spectrum.

Here, the speed of sound $c \propto \sqrt{T}$, T being the mean local atmospheric temperature, and $H \propto T/g$ is the pressure scale height of the atmosphere (Brown et al. 1991; Kjeldsen & Bedding 1995). Equation 2 suggests the use of a relation scaled to solar values of the form

$$\frac{\nu_{\max}}{\nu_{\max,\odot}} \simeq \frac{g}{g_{\odot}} \left(\frac{T_{\text{eff}}}{T_{\text{eff},\odot}} \right)^{-1/2}, \quad (3)$$

where, since oscillations are observed in the stellar photosphere, the temperature is set to $T = T_{\text{eff}}$. In this work, the solar values adopted are: $g_{\odot} = 27400 \text{ cm s}^{-2}$, $\nu_{\max,\odot} = 3090 \mu\text{Hz}$ and $T_{\text{eff},\odot} = 5777 \text{ K}$ (Chaplin et al. 2014).

Since all the stars considered in this work either have detected oscillations (real cohort) or would be predicted to show detected oscillations (synthetic cohort), ν_{\max} will typically be the parameter we choose to plot against when considering the noise properties of the stars.

First-order estimates of stellar mass and radius can be estimated using the above scaling relations. Combining and re-arranging Equation 1 and Equation 3 gives (Chaplin & Miglio 2013)

$$\frac{M}{M_{\odot}} = \left(\frac{\nu_{\max}}{\nu_{\max,\odot}} \right)^3 \left(\frac{\Delta\nu}{\Delta\nu_{\odot}} \right)^{-4} \left(\frac{T_{\text{eff}}}{T_{\text{eff},\odot}} \right)^{1.5}, \quad (4)$$

and

$$\frac{R}{R_{\odot}} = \left(\frac{\nu_{\max}}{\nu_{\max,\odot}} \right) \left(\frac{\Delta\nu}{\Delta\nu_{\odot}} \right)^{-2} \left(\frac{T_{\text{eff}}}{T_{\text{eff},\odot}} \right)^{0.5}. \quad (5)$$

With the basic global asteroseismic parameters defined, we now go on to explore the noise properties of stars in terms of these parameters. All noise components will be described up to the Nyquist frequency of the long-cadence *Kepler* data. The 29.4-minute cadence leads to a Nyquist frequency of $\nu_{\text{Nyq}} \approx 283 \mu\text{Hz}$ (Koch et al. 2010).

2.2 Modelling power due to the oscillations

For stars that have $\nu_{\max} \lesssim \nu_{\text{Nyq}}$, the power contained in the oscillations must be considered a component of the back-

ground signal for transit detection. It is sufficient to describe the contribution due to the oscillations in terms of a Gaussian of excess power centred around the frequency ν_{\max} (Equation 3). The width of the Gaussian is denoted by σ_{env} , as described by Equation 1 in Mosser et al. (2012a), i.e.,

$$\sigma_{\text{env}} = \frac{\delta_{\text{env}}}{2\sqrt{2\ln 2}}, \quad (6)$$

with δ_{env} describing the full width at half maximum (FWHM) of the oscillation envelope. The Gaussian also needs a height (maximum power spectral density), H , to give the final form of the oscillation envelope signature in the power spectrum:

$$\text{PSD}_{\text{osc}}(\nu) = H \exp\left[\frac{-(\nu - \nu_{\max})^2}{2\sigma_{\text{env}}^2} \right]. \quad (7)$$

The height and envelope width, H and δ_{env} , may be described in terms of scaling relations expressed in the parameter ν_{\max} (Mosser et al. 2012a), i.e.,

$$\begin{aligned} \delta_{\text{env}} &= 0.66(\nu_{\max})^{0.88} \\ H &= 2.03 \times 10^7 (\nu_{\max})^{-2.38} \text{ [ppm}^2 \mu\text{Hz}^{-1}]. \end{aligned} \quad (8)$$

As noted above, only the envelope describing the total oscillation power is considered and modelled. The power contained within individual modes is not required here. Returning to Figures 1 and 2, this envelope is plotted in red. With the oscillation contribution described, we move to describing the granulation parameters.

2.3 Granulation

A consequence of visible surface convection is granulation. As hot material rises on a plume, it cools at the surface and sinks back down. The stellar material forms cells, with a plume in the centre of each cell. Photometric granulation signatures for the Sun were initially modelled by Harvey (1985) as an exponentially decaying signal in the time domain. This is meant to represent the rapid rise in a convective plume, then the decay as the material cools. In photometric measurements this can be considered as the hotter material being intrinsically brighter, giving a brief spike in flux, before the material cools at the top of the plume, and grows dimmer, with the process occurring on some characteristic timescale.

This exponential in time leads to a Lorentzian when described in the power spectrum (in the frequency domain), and is known as a Harvey profile. Given that the exact nature of granulation is unclear, and that this simple formulation does not always appear to fit the granulation background well, this has in recent years led to a whole family of ‘‘Harvey-like’’ profiles (e.g., see Mathur et al. 2011), with varying formulations and exponents in the functions used. An important consideration for our work here is how granulation properties vary with stellar evolutionary state (once we have selected a preferred formulation). Does granulation in red giants exhibit the same behaviour as granulation observed in the Sun? In Kallinger et al. (2014), multiple models of granulation were fitted to power spectra over a range of stellar evolutionary states in cool stars to investigate updated versions of the original Harvey relation, including a change of exponent. Observed power spectra often require

the use of multiple granulation components, operating at different timescales, whereas the original Harvey model used only a single component, with an exponent of 2. We adopt a two-component granulation model, (described in Kallinger et al. 2014 as Model F) i.e.

$$\text{PSD}_{\text{gran}}(\nu) = \sum_{i=1}^2 \frac{\xi_i a_i^2 / b_i}{1 + (\nu/b_i)^4}. \quad (9)$$

Here ξ_i is a normalisation constant equal to $2\sqrt{2}/\pi$ for the model, while a_i and b_i are the granulation amplitude and characteristic frequency, respectively, of each granulation component, which are both dependent on the fundamental properties of the stars. Since the granulation and stellar oscillations are both driven by convection, it is perhaps not surprising that the granulation amplitude and frequency can be described by scaling relations based on asteroseismic parameters. In this case they are based on the frequency of maximum power ν_{max} , i.e., from Kallinger et al. (2014) we have:

$$\begin{aligned} a_1 &= a_2 = 3710(\nu_{\text{max}})^{-0.613}(M/M_{\odot})^{-0.26}, \\ b_1 &= 0.317(\nu_{\text{max}})^{0.97}, \\ b_2 &= 0.948(\nu_{\text{max}})^{0.992}, \end{aligned} \quad (10)$$

with an additional constraint from the stellar mass for the granulation amplitude (which may be derived from Equation 4, using ν_{max} , $\Delta\nu$ and T_{eff} as input). Whilst in Kallinger et al. (2014) both amplitude components (a_1 and a_2) were allowed to vary during the fitting procedure, the final relation produced used a single amplitude relation for both components. The mass-dependent formulation was also found to be a better fit to the real data, and as such is the formulation used here for the granulation amplitude. For the cohort of real asteroseismic stars considered below (see Section 3) we estimate stellar masses and radii using the scaling relations defined in Equations 4 and 5, with the solar value taken to be $135.1\mu\text{Hz}$ in this work (Chaplin et al. 2014)

Returning to Figure 1, the two granulation parameters plotted in blue, along with the oscillation envelope detailed above, make up the model power spectrum in red. Additionally, the shot noise component is plotted in green, clearly a small contribution in this power spectrum. It is from the model spectrum that we may compute a suitable noise metric for the star.

3 KEPLER CDPP

The primary *Kepler* noise metric is the CDPP, or Combined Differential Photometric Precision, which is designed to describe the noise properties of a star centred around a timescale of 6.5 hr (Christiansen et al. 2012; Gilliland et al. 2011). This is half the timescale on which an Earth analogue would transit a Sun-like star. Throughout the paper references to *Kepler* CDPP will refer to the 6.5 hr timescale. The CDPP will be composed of a shot noise component due to counting signals, but a significant stellar variability term should also be present. The nature of the stellar variability is dependent on the intrinsic stellar properties, with possible contributions from granulation, oscillations and activity.

Kepler lightcurves are produced in the Presearch Data Conditioning module (PDC) (Jenkins et al. 2010a; Smith

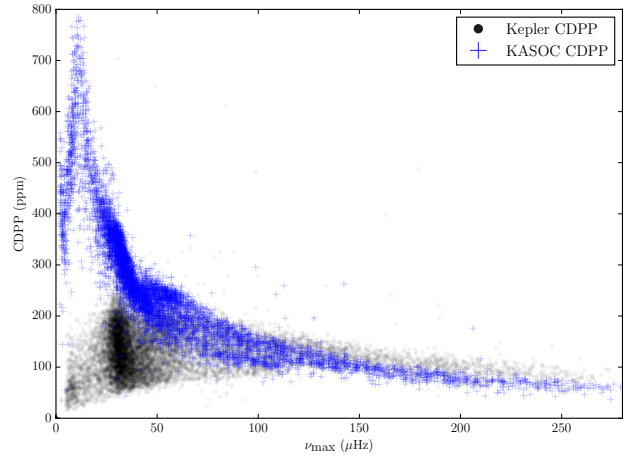


Figure 3. The reported CDPP for 13,000 evolved stars (Stello et al. 2013) plotted against the reported asteroseismic ν_{max} in black. The overall trend with decreasing ν_{max} is expected due to the increasing granulation amplitude (see Equation 10), but the turnover and spread below $100\mu\text{Hz}$ is evidence of the PDC pipeline removing astrophysical signal. Blue points are the result of work from KASOC (see text).

et al. 2012; Stumpe et al. 2012), and in general the PDC pipeline is highly successful at removing systematics and instrumental effects in the lightcurves. However the PDC also removes real astrophysical signal at long periods (Murphy 2014). This is of interest for evolved stars, having significant low-frequency signals typical of granulation and intrinsic oscillations. This loss of real signal has the effect of artificially reducing the reported CDPP, since real variability has been removed.

Figure 3 shows the reported CDPP for 13,000 red giants observed by *Kepler*. The reported CDPP appears to show increased scatter and attenuation at $\nu_{\text{max}} < 100\mu\text{Hz}$, i.e., in the more evolved stars in the cohort. The level of signal attenuation was explored by Gilliland et al. (2015) and Thompson et al. (2013). Long-period signals were injected into lightcurves, and attempts made to recover them after PDC processing. It was found that signals on timescales longer than a day showed attenuation. The scatter below $100\mu\text{Hz}$ in Figure 3 suggests that variability on timescales longer even than only 0.1 days will suffer some signal loss. Gilliland et al. (2015) also note that small-amplitude signals suffer more attenuation, in relative terms, than large-amplitude signals at the same frequency (period).

Taken at face value, Figure 3 suggests that some of the low ν_{max} (larger, more evolved) stars would be ideal for planet searches, since they appear to be photometrically quiet. However the turnover around $100\mu\text{Hz}$ is unphysical, a consequence of the PDC lightcurve processing (Thompson et al. 2013; Stumpe et al. 2014). This is the primary motivation to formulate an accurate model of the CDPP for evolved stars.

The data plotted in blue are the CDPP values calculated from lightcurves produced by an independent processing of the raw *Kepler* pixel data by the *Kepler* Asteroseismic Science Operations Center (KASOC) pipeline (Handberg & Lund 2014). This pipeline was intentionally designed to preserve astrophysical signal on longer timescales, and does not

show the same marked attenuation as the PDC data. As we shall now go on to discuss, our simple noise model – which is based on the scaling relations outlined above – is able to reproduce the observed KASOC CDPP values.

4 NOISE MODEL

Of the 13,000 stars in Figure 3, 6400 were identified as stars ascending the RGB (Elsworth, private comm). For each of these stars we constructed basic model power spectra up to the Nyquist frequency of $283 \mu\text{Hz}$. The granulation and oscillation power envelope contributions to the spectrum – which below we label as P_g and P_o – were modelled as in Sections 2.2 and 2.3, using the measured asteroseismic parameters (Stello et al. 2013) as input. The flat shot noise contribution P_s was modelled according to the upper envelope model described in Jenkins et al. (2010b). The RMS noise per long cadence in the time domain is

$$\sigma_s = \sqrt{c + 7 \times 10^7 / c}, \quad (11)$$

where

$$c = 3.46 \times 10^{0.4 \times (12 - Kp) + 8} \quad (12)$$

is the number of detected electrons per long cadence. The flat power-spectral density in the frequency domain then corresponds to:

$$P_s = 2 \times 10^{-6} \sigma_s^2 \Delta t \quad (13)$$

where Δt is the 29.4-minute cadence. Components due to the near-surface magnetic activity were not considered due to the evolved state of these stars. As we shall see below, this assumption appears to be validated by the good match of our model to the observations.

The model estimate of the CDPP may then be constructed as follows

$$\sigma_{\text{CDPP}} = \left(\Delta_T \int_0^{\nu_{\text{Nyq}}} F(\nu) \times [P_g + P_o + P_s] \right)^{0.5}, \quad (14)$$

where Δ_T is the resolution on which the artificial power spectra were computed and $F(\nu)$ represents the bandpass filter response for the model CDPP, which is comprised of high- and low-pass responses. As noted in Gilliland et al. (2011) the high-pass response may be described by a 2-day Savitsky-Golay filter (Savitzky & Golay 1964), whilst the low-pass response is a 6.5-hr sinc-squared function. The low-pass response ensures that the filter has zeros at harmonics of the 6.5-hr Earth-Sun half-transit duration, so that when constructing the noise metric transit signal is not included as misidentified stellar variability. The high-pass filter suppresses the model power spectral density around zero frequency. The filter has been tested against *Kepler* stars to ensure that the final values are similar to the PDC derived CDPP, for stars where no signal attenuation is occurs.

The attenuation of the signal due to the finite sampling time of *Kepler* is not considered here, due to the negligible influence of the effect around the region of the bandpass filter.

Figure 4 shows the main bandpass of the filter, whilst Figure 5 shows the filter imposed on a typical red giant power spectrum to indicate regions of the spectrum captured by the filter. Since the filter has higher-frequency structure,

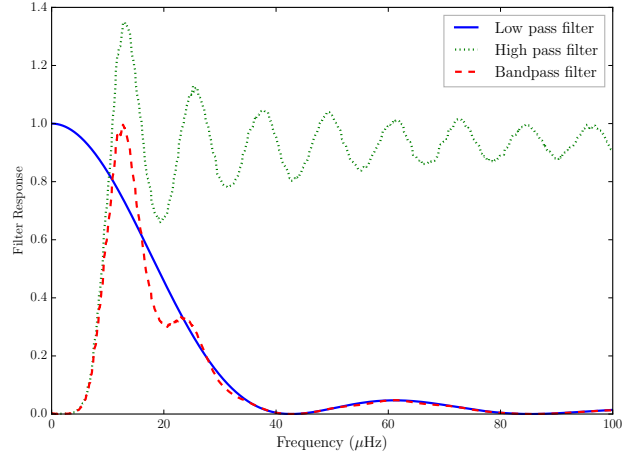


Figure 4. Filter response, with the Savitsky-Golay high-pass in green, 6.5-hr sinc-squared in blue, and the combined filter in red.

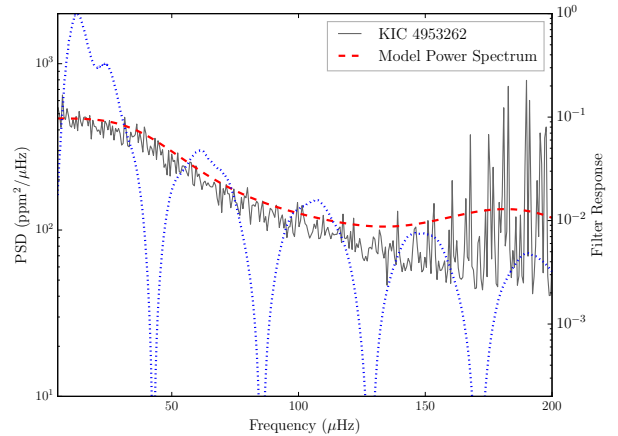


Figure 5. Filter response overplotted on KIC 4953262 power spectrum. Clearly most of the signal involved in the construction of the noise metric appears in the region $0 < \nu \lesssim 40 \mu\text{Hz}$. The filter response is shown on a log scale to emphasise regions of the power spectrum that contribute to the noise metric.

i.e., “ringing”, the CDPP of even low-luminosity red giants with ν_{max} values above $200 \mu\text{Hz}$ will have some contribution from the oscillations. However it should be clear that for low-luminosity red giants the primary contribution to the stellar noise will come from the stellar granulation, with the oscillations being a relatively minor, but not insignificant, contribution.

Figure 6 shows the model-estimated CDPP values in red, overlaid on the observed CDPP values from Figure 3, (PDC pipeline CDPP values in black and the KASOC pipeline CDPP values in blue). We see good agreement between the model and the observed KASOC pipeline values. This is a clear indication that the model used is sufficiently robust, and additionally that a stellar activity component is not required for these stars. The turnover around $10 \mu\text{Hz}$ is due to the oscillation envelope passing through the frequency bandpass of the filter. The additional scatter seen

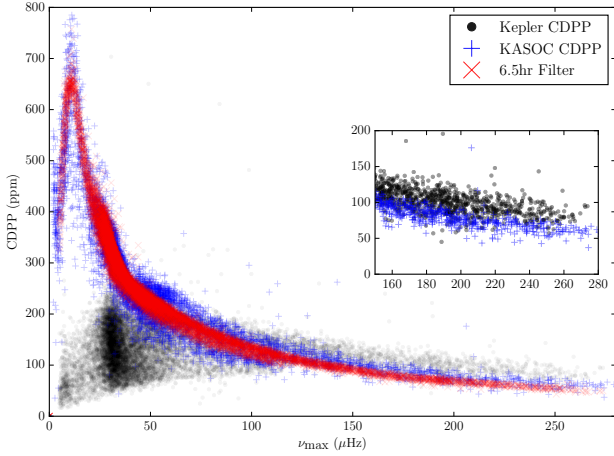


Figure 6. The model CDPP shows a strong trend with ν_{\max} . Stars at lower ν_{\max} represent larger stars, with larger granulation signal, since the amplitude scales with ν_{\max} (see Eq 10). At low frequencies around $10\mu\text{Hz}$, the contribution from the stellar oscillations is of the same order as the granulation background. The KASOC results are also reproduced and show good agreement with the model results. The inset focuses on the high ν_{\max} ($\nu_{\max} > 150\mu\text{Hz}$) stars, and shows that the KASOC results show significantly less noise than the PDC derived CDPP.

in the KASOC results around $50\mu\text{Hz}$ is due to the presence of RC stars, which do not obey the scaling relations used in construction of power spectra in the same way as stars on the RGB, we therefore removed these stars in the work that follows. The clump stars were also removed due to the assumption that upon ascent up the RGB, any existing low period planetary system will have been engulfed by the star. As such they are of little relevance when considering the potential planet yield left in *Kepler* data.

Figure 7 also demonstrates that the intrinsic stellar oscillations are a key component of the stellar noise for low ν_{\max} , high-luminosity RGBs. In the region around the turnover ($\nu \approx 10\mu\text{Hz}$) in Figure 6, the signal from oscillations dominates by a factor of ~ 1.5 ; there is also an enhancement in the oscillation contribution around the first ringing of the filter at $60\mu\text{Hz}$ because this is where the oscillation envelope passes through the filter (with ν_{\max} aligning with a local maximum in the filter bandpass). It is important to note that even when granulation is the dominant noise source, the stellar oscillations remain a significant factor.

Finally, it should be noted from Figure 6 that low-luminosity giants near the base of the RGB show lower noise in the KASOC pipeline data than in the PDC data, as highlighted in the inset. This would have consequences for the detection yield from these stars.

Having established earlier that our model does a good job of describing the intrinsic stellar noise for evolved stars, we go on to apply this CDPP to estimate the minimum detectable planet radii around red giant stars in *Kepler* data.

4.1 Minimum Radius detection

The canonical *Kepler* CDPP is designed to capture the noise properties around a 6.5-hr timescale, related to the transit timescale of an Earth analogue. But is this filter appropriate

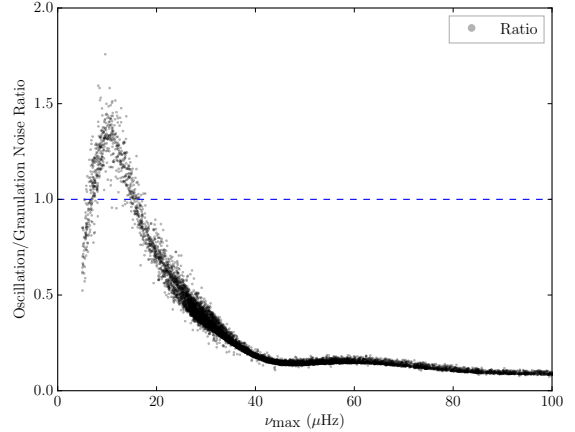


Figure 7. The ratio of the contribution to the model CDPP between oscillations and granulation, for 6400 known red giants. The dashed line marks unity.

to the red-giant case? The basic form of the transit duration equation (Seager & Mallén-Ornelas 2003; Winn 2010) is

$$t_{\text{dur}} = \frac{R_{\star}P}{\pi a} (1 - b^2)^{0.5}, \quad (15)$$

where P is the orbital period, a is the semi-major axis, and b is the impact parameter, and there is the implicit assumption of circular orbits. This may be re-written in the form:

$$t_{\text{dur}} = \left[\frac{4R_{\star}^2 a}{GM_{\star}} (1 - b^2) \right]^{0.5}. \quad (16)$$

The maximum transit duration (for $b = 0$) is therefore proportional to $R_{\star}a^{0.5}$. This can potentially vary anywhere from an Earth-analogue duration (e.g., Kepler-56b, a short-period planet around another low luminosity red giant, with a transit duration of 13.3hrs) up to durations exceeding one day (e.g., wide orbits around low-luminosity RGB stars, or closer orbits around more evolved giants).

Since the range of possible transit durations is so broad for stars ascending the RGB, the noise properties being considered need to capture the stellar variability over the relevant timescales. A 6.5-hr filter turns out to be more appropriate than it might at first seem. To explain why, we return to Figure 4. The maximum of the bandpass of the filter is at $12.5\mu\text{Hz}$, a timescale of around 22 hours. The half power points of the bandpass lie at $9.2\mu\text{Hz}$ and $16.6\mu\text{Hz}$, corresponding to 30.2 and 16.7 hours respectively. There is also a significant contribution to the bandpass at even shorter periods (i.e., note the secondary peak at around $25\mu\text{Hz}$, which corresponds to about 11 hours). As we shall see below, because the chances of detecting planets around very evolved red giants – where transit durations would be much longer than a day – are so low, our numbers above indicate that the current filter already does a reasonable job of capturing the necessary timescales of interest for transits of lower luminosity red giants.

The CDPP values from our model as inputs to calculate a minimum detectable planet radius for each of the *Kepler* RGB stars, according to Equation 1 in Howard et al. (2012):

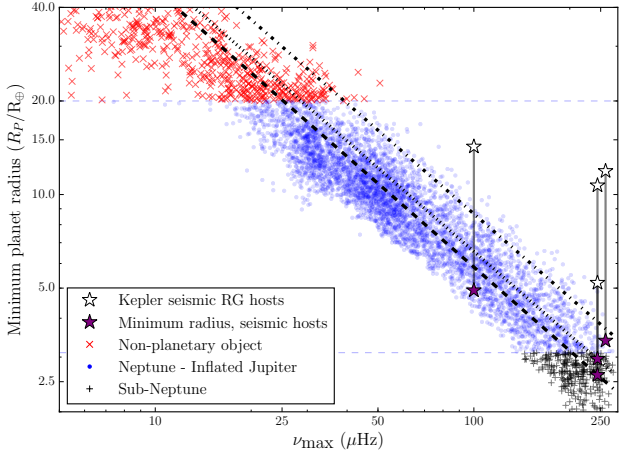


Figure 8. Minimum detection radius in Earth radii, for the 6400 *Kepler* stars. Clearly this is a strong function of ν_{\max} , in this case a proxy for stellar radius. The diagonal lines are fits to a power-law relation between ν_{\max} and R_{\min} for assumed periods of 10 days (dashed), 20 days (dotted) and 100 days (dot-dashed). Radii of known planets (open stars) and the corresponding estimated minimum radii (filled stars) for the same systems are also shown, connected by vertical black lines. Points and crosses indicate the minimum radii for illustrative distribution described in the text

$$R_{\min} = R_{\star} (\text{SNR} \times \sigma_{\text{CDPP}})^{1/2} \left(\frac{6.5 \text{hr}}{n_{\text{tr}} t_{\text{dur}}} \right)^{1/4}, \quad (17)$$

The assumed detection signal-to-noise ratio was taken as $\text{SNR}=10$, this value is adopted as a “secure” detection threshold. This is stronger than the 7.1σ threshold used in the *Kepler* mission for transit detections (Jenkins et al. 2010a) to ensure these planets would be detected (see Borucki et al. 2011; Howard et al. 2012; Fressin et al. 2013; Christiansen et al. 2013).

The transit duration was calculated according to Equation 15, taking $b = 0$; the stellar radius was taken to be the asteroseismically determined value from Equation 5; and n , the number of observed transits, was assumed to equal $n = 4\text{yr}/\text{Period}(\text{yr})$, rounded down to the nearest integer. The factor of 6.5 in Equation 17 accounts for the timescale on which the CDPP is calculated compared to the transit duration. It should also be noted that the 4-year factor in the number of transits assumes all stars were observed continuously for the entire duration of the *Kepler* mission, any missing transits would increase the minimum detectable radius.

The diagonal lines in Figure 8 show power-law fits to ν_{\max} of the calculated minimum detection radii R_{\min} of the 6400 *Kepler* stars, assuming fixed orbital periods of 10 days (dashed line), 20 days (dotted line) and 100 days (dot-dashed line), respectively. The vertical offset seen between the diagonal lines is due to the reduced number of transits seen for longer period planets. The minimum radii here were calculated using the model CDPP predictions. But we could also have used the KASOC CDPP data, which give very similar results. The true, underlying period distribution for planets orbiting evolved hosts is of course very poorly constrained. For illustrative purposes only, we have also calculated mini-

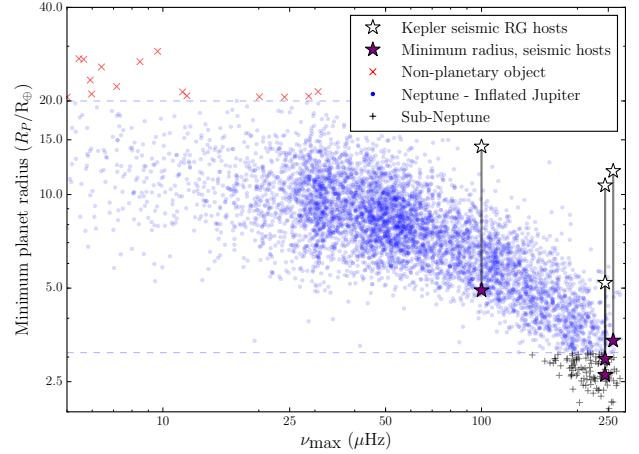


Figure 9. Minimum detection radius in Earth radii, if the PDC CDPP results are used. Again the 20 day distribution has been used here. Clearly the PDC results would suggest that planets would be detectable around low ν_{\max} stars, but this is purely an effect of the PDC processing producing anomalously low CDPP values.

um radii using an underlying distribution that is consistent with results on confirmed *Kepler* planets, with data taken from the NASA Exoplanet Archive (Akeson et al. 2013)¹. These data are well described by a log-normal distribution, with the underlying normal distribution having a mean and standard deviation of 2.47 and 1.23 in $\log_e P$. The results are plotted on Figure 8, blue dots are super-Earth to Jupiter sized objects, whilst red crosses are objects with minimum radii greater than that which is feasible for a planet. Black crosses indicate a minimum radii of less than the radius of Neptune.

Figure 8 shows that even the most inflated hot-Jupiter planets will be undetectable around high RGB stars (i.e., stars with low ν_{\max}). This is due to the large radii of these stars, and the resulting small transit depths. Due to the inflated nature of the stars themselves, finding Earth-like planets at high SNR will most likely prove unfeasible across the entire population of evolved stars. For low-luminosity red giants, there is the potential to reach super-Earth sized planets. However it is apparent that the focus for planets around red-giant hosts should be Neptune to Jupiter-sized giant planets.

Radii of known planets (open stars) and the estimated minimum radii (filled stars) for the same systems are also shown on Figure 8, connected by vertical black lines. As can also be seen, the currently known transiting planets around evolved hosts sit on the upper edge of the distribution in planet radius and ν_{\max} . The lack of detections around low- ν_{\max} stars suggests that any systematic search for planets around evolved hosts should instead concentrate on low-luminosity RGB stars. We note that we might expect radii for actual detections to cover a range of radii at and above the minimum radii and this is what we see in Figure 8, albeit for a very small sample.

Figure 9 shows the same minimum radius calculation

¹ <http://exoplanetarchive.ipac.caltech.edu/>

using the current *Kepler* PDC derived CDPF values. These results would (incorrectly) suggest that planets could be detected around low ν_{\max} stars due to the aforementioned attenuation of intrinsic stellar signals on long timescales. For the high ν_{\max} stars, the minimum radii are also larger than the results for the for updated noise model CDPF described here.

As stars ascend the RGB, planets on short periods are rapidly engulfed by the expanding star. Additionally the tidal decay timescale decreases for evolved stars (Schlaufman & Winn 2013), e.g., the Kepler-56 system, where the planets are likely to be engulfed within ~ 100 Myr (Li et al. 2014). Even without consideration of tidal decay, for the case of evolved RGB hosts, planets on short periods, and many cases in the *Kepler* period distribution described above, would have to exist inside the stellar envelope (these cases have been removed from Figure 8).

4.2 Transit Injection Test

To ensure the results for the minimum detection radius in Figure 8 are reasonable, a sensible test was to inject transit signals into real *Kepler* data and attempt to recover the transit signal. As an example a red giant with similar stellar and asteroseismic properties ($\nu_{\max} = 255\mu\text{Hz}$) to Kepler-56, but with no known transits, was selected and a transit signal injected into the detrended lightcurve. A planet with the minimum detection radius ($R_{\min} = 2.25R_{\oplus}$, for a planet on a 20 day orbit, at $\text{SNR}=10$) was injected into the lightcurve on a 20 day orbit, and was recovered using a box-least squares algorithm² (Kovács et al. 2002) at the required SNR threshold. Figure 10 shows the injected transit in the lightcurve, folded on the period of the injected planet (grey points). Also shown is the re-binned lightcurve after folding on the period of the planet (blue points) and the model for the injected transit (red line).

This is of particular importance since the current sample of known transiting planets around evolved hosts in the NASA Exoplanet Archive all have a detection $\text{SNR} \geq 15$. Returning once more to Kepler-56, the detection ratios in that system are 63 and 44, for planets b and c respectively. However as the BLS injection test shows, smaller planets are recoverable in the data. The transit injection performed here, along with the minimum planet radii calculated above, suggest that Neptune-sized planets should be detectable in the *Kepler* lightcurves of low-luminosity, red-giant stars, if they are present.

5 CONCLUSIONS

In this work we have presented a simple model to describe the noise properties of evolved stars as relevant to transit searches for exoplanets. Our model predictions of the commonly-used *Kepler* CDPF noise metric is dominated for evolved stars by granulation and oscillations. It includes a significant contribution from stellar oscillations, with the solar-like oscillations representing the dominant noise source

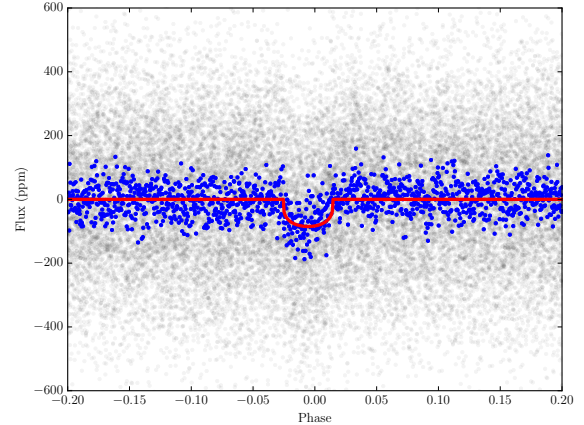


Figure 10. Injected transit into *Kepler* detrended lightcurve, folded on the 20 day period of injected planet (black). Also plotted is binned lightcurve, folded on period (blue), along with model for the planet injection (red)

for any photometric survey of stars near the tip of the red-giant branch. Importantly, our model also recovers the appropriate noise signatures for highly evolved stars, a feature not shared by current *Kepler* results. This noise model may be applied to the predictions of the noise properties of evolved stars for the upcoming TESS and PLATO missions.

As a simple application of this updated CDPF, we also estimated minimum detectable planet radii for low-luminosity red giants, for different assumed orbital periods. The results suggest that Neptune-sized planets on short-period ($P \leq 20$ days) orbits should be detectable in the *Kepler* data. We advocate a detailed search for planets around red giants. Giant planets around evolved stars will also be detectable in lightcurves from the upcoming TESS mission (Ricker et al. 2014) as well as the ongoing K2 mission, which has already targeted a dedicated sample of several thousand low-luminosity red giants to detect giant planets (Huber 2015, Grunblatt et al., submitted).

ACKNOWLEDGEMENTS

Funding for this Discovery mission is provided by NASA’s Science Mission Directorate. The authors wish to thank the entire Kepler team, without whom these results would not be possible. T.S.H.N., W.J.C. and T.L.C. acknowledge financial support from the UK Science and Technology Facilities Council (STFC). Funding for the Stellar Astrophysics Centre is provided by The Danish National Research Foundation (Grant agreement no.: DNR106), M.N.L. acknowledges the support of The Danish Council for Independent Research | Natural Science (Grant DFF-4181-00415). The research is supported by the ASTERISK project (ASTERoseismic Investigations with SONG and Kepler) funded by the European Research Council (Grant agreement no.: 267864).

T.S.H.N. would also like to acknowledge Yvonne Elsworth for the identification of *Kepler* RGB stars. D.H. acknowledges support by the Australian Research Council’s Discovery Projects funding scheme (project number DE140101364) and support by the National Aeronautics

² python implementation of BLS created by Dan Foreman-Mackey and Ruth Angus <https://github.com/dfm/python-bls>

and Space Administration under Grant NNX14AB92G issued through the *Kepler* Participating Scientist Program.

REFERENCES

- Adamów M., Niedzielski A., Villaver E., Nowak G., Wolszczan A., 2012, *ApJ*, **754**, L15
- Akeson R. L., et al., 2013, *PASP*, **125**, 989
- Barclay T., Endl M., Huber D., Foreman-Mackey D., Cochran W. D., MacQueen P. J., Rowe J. F., Quintana E. V., 2015, *ApJ*, **800**, 46
- Baudin F., et al., 2011, *A&A*, **529**, A84
- Bedding T. R., et al., 2011, *Nature*, **471**, 608
- Belkacem K., Goupil M. J., Dupret M. A., Samadi R., Baudin F., Noels A., Mosser B., 2011, *A&A*, **530**, A142
- Borucki W. J., et al., 2011, *ApJ*, **736**, 19
- Brown T. M., Gilliland R. L., Noyes R. W., Ramsey L. W., 1991, *ApJ*, **368**, 599
- Campante T. L., et al., 2015, *ApJ*, **799**, 170
- Chaplin W. J., Miglio A., 2013, *ARA&A*, **51**, 353
- Chaplin W. J., et al., 2014, *ApJS*, **210**, 1
- Christiansen J. L., et al., 2012, *PASP*, **124**, 1279
- Christiansen J. L., et al., 2013, *ApJS*, **207**, 35
- Ciceri S., Lillo-Box J., Southworth J., Mancini L., Henning T., Barrado D., 2015, *A&A*, **573**, L5
- Fressin F., et al., 2013, *ApJ*, **766**, 81
- Gilliland R. L., et al., 2011, *ApJS*, **197**, 6
- Gilliland R. L., Chaplin W. J., Jenkins J. M., Ramsey L. W., Smith J. C., 2015, *AJ*, **150**, 133
- Handberg R., Lund M. N., 2014, *MNRAS*, **445**, 2698
- Harvey J., 1985, in Rolfe E., Battrick B., eds, ESA Special Publication Vol. 235, Future Missions in Solar, Heliospheric & Space Plasma Physics.
- Hekker S., et al., 2011, *MNRAS*, **414**, 2594
- Howard A. W., et al., 2012, *ApJS*, **201**, 15
- Huber D., 2015, preprint, ([arXiv:1511.07441](https://arxiv.org/abs/1511.07441))
- Huber D., et al., 2013, *Science*, **342**, 331
- Jenkins J. M., et al., 2010a, *ApJ*, **713**, L87
- Jenkins J. M., et al., 2010b, *ApJ*, **713**, L120
- Johnson J. A., Marcy G. W., Fischer D. A., Wright J. T., Reffert S., Kregenow J. M., Williams P. K. G., Peek K. M. G., 2008, *ApJ*, **675**, 784
- Kallinger T., et al., 2014, *A&A*, **570**, A41
- Kjeldsen H., Bedding T. R., 1995, *A&A*, **293**
- Koch D. G., et al., 2010, *ApJ*, **713**, L79
- Kovács G., Zucker S., Mazeh T., 2002, *A&A*, **391**, 369
- Li G., Naoz S., Valsecchi F., Johnson J. A., Rasio F. A., 2014, *ApJ*, **794**, 131
- Lillo-Box J., et al., 2014, *A&A*, **562**, A109
- Mathur S., et al., 2011, *ApJ*, **741**, 119
- McQuillan A., Mazeh T., Aigrain S., 2014, *ApJS*, **211**, 24
- Mosser B., et al., 2012a, *A&A*, **537**, A30
- Mosser B., et al., 2012b, *A&A*, **540**, A143
- Murphy S., 2014, Investigating the A-Type Stars Using Kepler Data. Springer Theses, Springer International Publishing, <https://books.google.co.uk/books?id=HfusbAAQBAJ>
- Quinn S. N., et al., 2015, *ApJ*, **803**, 49
- Quirrenbach A., Reffert S., Trifonov T., Bergmann C., Schwab C., 2015, in AAS/Division for Extreme Solar Systems Abstracts. p. 502.01
- Reffert S., Bergmann C., Quirrenbach A., Trifonov T., Künstler A., 2015, *A&A*, **574**, A116
- Ricker G. R., et al., 2014, in Society of Photo-Optical Instrumentation Engineers (SPIE) Conference Series. p. 20 ([arXiv:1406.0151](https://arxiv.org/abs/1406.0151)), doi:10.1117/12.2063489
- Savitzky A., Golay M. J. E., 1964, *Analytical Chemistry*, **36**, 1627
- Schlafman K. C., Winn J. N., 2013, *ApJ*, **772**, 143
- Schröder K.-P., Connon Smith R., 2008, *MNRAS*, **386**, 155
- Seager S., Mallén-Ornelas G., 2003, *ApJ*, **585**, 1038
- Silva Aguirre V., et al., 2015, *MNRAS*, **452**, 2127
- Smith J. C., et al., 2012, *PASP*, **124**, 1000
- Steffen J. H., et al., 2013, *MNRAS*, **428**, 1077
- Stello D., et al., 2013, *ApJ*, **765**, L41
- Stumpe M. C., et al., 2012, *PASP*, **124**, 985
- Stumpe M. C., Smith J. C., Catanzarite J. H., Van Cleve J. E., Jenkins J. M., Twicken J. D., Girouard F. R., 2014, *PASP*, **126**, 100
- Thompson S. E., Christiansen J. L., Jenkins J. M., Caldwell D. A., Barclay T., Bryson S. T., Burke C. J., Campbell J. R., 2013, Kepler Data Release 21, (KSCI-19061-001)
- Ulrich R. K., 1986, *ApJ*, **306**, L37
- Van Eylen V., et al., 2014, preprint, ([arXiv:1412.4848](https://arxiv.org/abs/1412.4848))
- Winn J. N., 2010, preprint ([arXiv:1001.2010](https://arxiv.org/abs/1001.2010))

This paper has been typeset from a $\text{\TeX}/\text{\LaTeX}$ file prepared by the author.